

FBQ 0951+2635: time delay and structure of the main lensing galaxy

Vyacheslav N. Shalyapin^{1,2,3}, Luis J. Goicoechea^{1,2}, and Eleana Ruiz-Hinojosa²

¹ Instituto de Física de Cantabria (CSIC-UC), Avda. de Los Castros s/n, E-39005 Santander, Spain
e-mail: vshal@ukr.net, goicol@unican.es

² Departamento de Física Moderna, Universidad de Cantabria, Avda. de Los Castros s/n, E-39005 Santander, Spain

³ O.Ya. Usikov Institute for Radiophysics and Electronics, National Academy of Sciences of Ukraine, 12 Acad. Proscury St., UA-61085 Kharkiv, Ukraine

December 13, 2024

ABSTRACT

As there is a long-standing controversy over the time delay between the two images of the gravitationally lensed quasar FBQ 0951+2635, we combined early and new optical light curves to robustly measure a delay of 13.5 ± 1.6 d (1σ interval). The new optical records covering the last 17 yr were also used to trace the long-timescale evolution of the microlensing variability. Additionally, the new time delay interval and a relatively rich set of further observational constraints allowed us to discuss the mass structure of the main lensing galaxy at redshift 0.26. This lens system is of particular interest because the external shear from secondary gravitational deflectors is relatively low, but the external convergence is one of the highest known. When modelling the galaxy as a singular power-law ellipsoid without hypotheses/priors on the power-law index, ellipticity and position angle, we demonstrated that its mass profile is close to isothermal, and there is good alignment between mass and near-IR light. We also recovered the true mass scale of the galaxy. Finally, it is worth mentioning that a constant mass-to-light ratio model also worked acceptably well.

Key words. galaxies: structure – gravitational lensing: strong – quasars: individual: FBQ 0951+2635

1. Introduction

Strong gravitational lensing at the galaxy scale is a key tool to investigate the structure of non-local early-type galaxies (e.g., Koopmans et al. 2006; Shajib et al. 2024). If the lensed source is a quasar, the mass distribution of the main lensing galaxy can be probed with a suitable number of observational constraints. Although deep photometric observations with the *Hubble Space Telescope* (HST) or ground-based facilities incorporating adaptive optics provide images of the quasar host galaxy (e.g., Wong et al. 2020), the basic constraints consist of the positions of the quasar images and the light distribution of the main lens. In addition to these basic astro-photometric data, deep spatially-resolved spectroscopy of the system is required to estimate unbiased macro-magnification ratios, i.e., flux ratios between quasar images that are not affected by extinction, microlensing, and intrinsic variability effects (e.g., Sluse et al. 2012b; Goicoechea & Shalyapin 2016). Radio fluxes, if available, are expected to be unaffected by microlensing (large source) and dust extinction (long wavelength), and thus radio flux ratios at a single epoch are good proxies of the macro-magnification ratios for a lensed quasar with short delays between images. Sometimes, a smoothly-distributed lensing mass fails to reproduce measured macro-magnification ratios of a lensed quasar, and these flux ratio anomalies may be caused by the galaxy substructures (millilensing; e.g., Metcalf & Madau 2001). Millilensing effects would be different for broad emission lines, radio fluxes and narrow emission lines because they depend on the source size (e.g., Moustakas & Metcalf 2003).

According to Refsdal’s 60-year old ideas (Refsdal 1964), the time delays between quasar images from photometric monitor-

ing campaigns can also be used to constrain the mass distribution of the main lens, provided that spectroscopic redshifts of the source and main lens are known, and the main cosmological parameters are derived from independent experiments (e.g., Hinshaw et al. 2009; Planck Collaboration VI 2020). Additionally, information about the stellar kinematics of the main lens, or about the secondary deflectors around the main one and along the line of sight is required to reliably probe the mass distribution of the main lensing galaxy (e.g., Falco et al. 1985; Suyu et al. 2010). At present, this last information is only available for a relatively small number of lensed quasars with detailed studies on the stellar kinematics of their main lenses (e.g., Birrer et al. 2020; Shajib et al. 2023), or on main lens environments and line-of-sight deflectors (e.g., Rusu et al. 2017; Wilson et al. 2017).

FBQ 0951+2635 is a doubly imaged quasar that was discovered by Schechter et al. (1998). This lensed quasar is located at a redshift $z_s = 1.249$ (Momcheva et al. 2015), and the main lens is an early-type galaxy at $z_l = 0.260$ (Eigenbrod et al. 2007). It is a particularly interesting lens system for several reasons. First, even though near-IR HST imaging of FBQ 0951+2635 (Kochanek et al. 2000) led to two formally precise solutions for the relative astrometry of the system and the morphology of the early-type galaxy (Jakobsson et al. 2005; Sluse et al. 2012a), these solutions are not consistent with each other. Thus, we aim to study how both astro-photometric datasets influence the reconstruction of the lensing mass. Although the near-IR morphology of the galaxy basically consists of a prominent elliptical halo, very recently, Rivera et al. (2023) have suggested the existence of an additional feature: a faint edge-on disc. In this paper, we do not consider the presence of minor features requiring confirmation through new observations. Second, there

arXiv:2412.09435v1 [astro-ph.GA] 12 Dec 2024

are spectroscopic observations with large optical telescopes in very good seeing conditions and radio fluxes at 3.6 cm from the Very Large Array (VLA) that can be used to obtain a reliable constraint on the macro-magnification ratio (e.g., Jakobsson et al. 2005; Sluse et al. 2012b). Third, Wilson et al. (2017) quantified the gravitational lensing effect of galaxy groups at the main lens redshift and along the line of sight.

We also aim to use the time delay between both quasar images as an important constraint on the mass distribution of the non-local early-type galaxy. However, current values of the time delay of FBQ 0951+2635 are not trustworthy. Optical light curves in the period 1999–2001 were initially analysed by Jakobsson et al. (2005), who obtained a time delay of 16 ± 2 d (the brightest image is leading) using the last 38 data points. Despite these last data seem to be weakly affected by extrinsic (microlensing) variability, an iterative fit yielded a time delay of 13 ± 4 d using all (58) data points, i.e., having twice the uncertainty and a significantly shorter central value. From the same dataset, Eulaers & Magain (2011) found that different time delay values in the 10–30 d interval are possible, whereas Rathna Kumar et al. (2015) measured a time delay of 7.8 ± 14.0 d. The obvious conclusion is that additional data are required to reliably measure the time delay of the system.

The paper is organized as follows. In Sect. 2, we analyse optical light curves of FBQ 0951+2635 spanning 25 yr (1999–2024) to determine a reliable time delay between the two quasar images and identify the long-term microlensing signal. Sect. 3 includes the observational constraints for the lens system, as well as the methodology to probe the mass distribution of the main lensing galaxy and the results on its structure. In Sect. 4, we present our main conclusions.

2. Optical light curves and time delay

2.1. Light curves

The first optical monitoring campaigns of FBQ 0951+2635 focused on the *R* passband. Thus, based on observations with the Nordic Optical Telescope (NOT) at 58 epochs (nights), Jakobsson et al. (2005) and Paraficz et al. (2006) presented *R*-band light curves of the two quasar images (A and B) from 1999 to 2001. A monitoring programme with the main Maidanak Telescope (MT) in the period 2001–2006 also led to *R*-band light curves at 37 epochs (Shalyapin et al. 2009).

After the pioneering variability records from NOT and MT observations, as part of the GLENDAMA project (Gil-Merino et al. 2018), we have monitored FBQ 0951+2635 with the Liverpool Telescope (LT) in the optical *r* band from 2009 to 2024. Over the full monitoring period, *r*-band magnitudes at 142 epochs have been obtained (the photometric model and initial LT light curves were presented by Gil-Merino et al. 2018). We then combined the LT magnitudes and those obtained with the Kaj Strand Telescope (KST) during 2008–2017 (Rivera et al. 2023), removing two KST epochs at MJD = 54883 and 57866 with possible outliers, correcting small magnitude offsets between the Tek2k and OneChip cameras in the KST (image A and B offsets of -0.001 and $+0.005$ mag for OneChip respect to Tek2k), and shifting the KST magnitudes to the LT system ($+16.879$ and $+16.809$ mag for A and B, respectively). We point out that magnitude offsets are estimated in a standard way by comparing concurrent data from two different cameras/telescopes. In addition, photometric errors rely on the intra-night magnitude scatter drawn from the analysis of two or three individual frames each

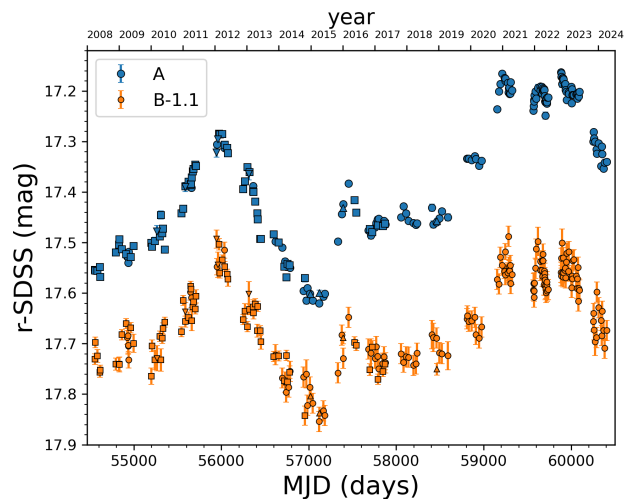


Fig. 1. GLENDAMA+ light curves of FBQ 0951+2635. These new variability records mainly consist of photometric data from the LT (circles) and KST (squares), but also incorporate information provided by the PS (inverted triangles) and DES (triangles) databases. See main text for details.

night. Possible outliers are also removed as they may have an impact on time delay measurements.

To improve the sampling over the period 2008–2024, we added several *r*-band magnitudes (LT photometric system) in the Data Release 1 of Pan-STARRS¹ (PS; Flewelling et al. 2020) and the Data Release 2 of the Dark Energy Survey² (DES; Abbott et al. 2021). The new 17-yr brightness records including magnitudes at 213 epochs are available in Table 1 at the CDS. These LT-KST-PS-DES (GLENDAMA+) light curves are also displayed in Figure 1.

2.2. Time delay measurement

The *R*-band NOT light curves did not permit to measure a time delay between A and B with a precision of $\sim 10\%$. The analysis of Jakobsson et al. (2005) suggested a delay interval of 10–20 d (depending on the technique, the smoothing, and the data points used), and subsequent studies indicated delay intervals of 10–30 d (Eulaers & Magain 2011) and even including negative values, i.e., image B leads image A (Rathna Kumar et al. 2015). Hence, additional light curves are required to address time delay measurements to $\sim 10\%$, and here we consider the NOT dataset along with the GLENDAMA+ one. There is clear evidence for intrinsic variations in the 2008–2024 period, since brightness changes of A and B are significantly greater than photometric uncertainties, and additionally, A and B have an almost parallel behaviour (see Figure 1).

Because the optical light curves of FBQ 0951+2635 are affected by a long-timescale microlensing episode (e.g., Shalyapin et al. 2009; Rivera et al. 2023), we measured the time delay using cross-correlation techniques that account for extrinsic variability. We have developed easy-to-use Python scripts to estimate the time delay of a doubly imaged quasar from two different methods incorporating polynomial microlensing variability. These scripts are publicly available at GitHub³ and briefly described in Appendix A. The first method we have used is the

¹ <http://panstarrs.stsci.edu>

² <https://www.darkenergysurvey.org>

³ https://github.com/glendama/q0951time_delay

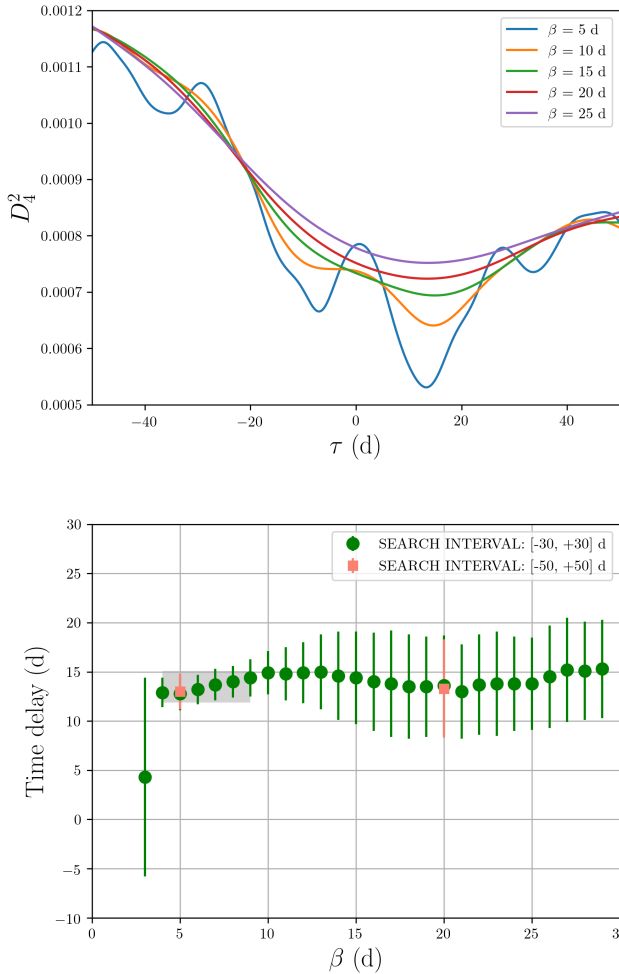


Fig. 2. Time delay estimation from the dispersion technique. Dispersion spectra D_4^2 are based on a Gaussian weighting function whose width is described by the parameter β , as well as a microlensing polynomial of degree five ($N_{\text{ml}} = 5$; see main text). *Top panel:* D_4^2 spectra using the NOT light curves plus the new GLENDAMA+ brightness records and five values of β . These spectra have minima at time lags $\tau = 13$ – 15 d. *Bottom panel:* 1σ confidence intervals for the time delay using 1000 synthetic light curves of each image and a large set of β values. A combined measurement from the six delay intervals for $\beta = 4$ – 9 d is highlighted with a light-grey rectangle encompassing the individual measurements.

most sophisticated variant of the dispersion technique (D_4^2 ; Pelt et al. 1996), which relied on a weighting scheme for the squared differences between the B image data and shifted A image data, where the A image data were shifted by a time lag τ and a microlensing polynomial of degree N_{ml} . Our Gaussian weighting scheme was characterised by a parameter β and is outlined in Appendix A. After setting values for N_{ml} and β , the dispersion spectrum D_4^2 was computed as the weighted sum of squared differences for time lags within a reasonable interval. To build this spectrum, we previously solved the microlensing polynomial coefficients that minimise it for each τ value. The time delay is assumed to be the time lag that minimises the dispersion spectrum.

Considering polynomials of different degrees and several values of the parameter β , we verified that minimum dispersions decrease when the polynomial degree is progressively increased up to $N_{\text{ml}} = 5$, while a polynomial of degree $N_{\text{ml}} = 6$ does not produce substantial decreases in minimum dispersions. For N_{ml}

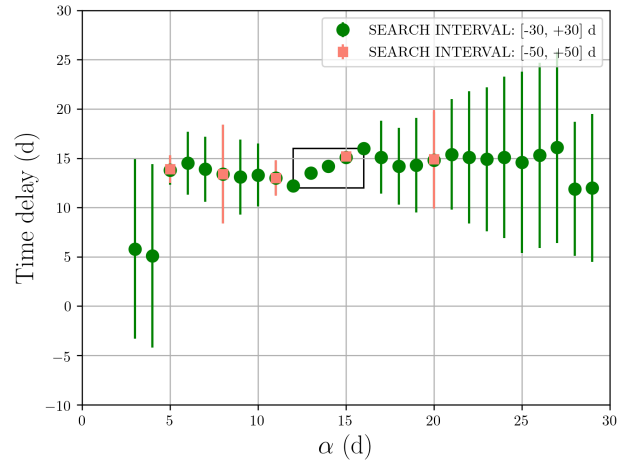


Fig. 3. Time delay estimation from the chi-square technique and 1000 synthetic light curves of each quasar image. To match light curves of the two images, a microlensing polynomial of degree five and binned light curves of B are considered, where bins of the B image have a semisize α . The error bars represent 1σ confidence intervals for the time delay, and the black outlined rectangle contains five anomalous measurements (see main text).

= 5 and a broad range of β values ($3 < \beta < 30$ d), we found stable minima in the D_4^2 spectra covering the time lag interval $[-50, +50]$ d. Some of these spectra with minima at 13–15 d are shown in the top panel of Figure 2.

To quantify delay uncertainties, we generated 1000 synthetic light curves of each image based on the observed records (e.g., Shalyapin & Goicoechea 2017). More precisely, we made 1000 "repetitions of the experiment" (synthetic curves for A and B) by adding random quantities to the measured magnitudes. These random quantities were realisations of normal distributions around zero, with standard deviations equal to the measured errors. We do not exactly repeat the original experiment but rather a worsened experiment with errors greater than those observed, that is, simulated magnitudes are not derived through a reconstruction of the underlying signal but from the observed one. Our simulation scheme is thus conservative regarding the size of error bars (about 20% larger than the measured ones), with the caveat that only uncorrelated noise is added. We obtained distributions of time lags and polynomial coefficients that minimise the D_4^2 spectra from the simulated records. We then searched for minima within the interval $[-30, +30]$ d to speed up numerical calculations involving thousands of dispersion spectra. However, for certain β values, we checked that results using this narrower range of time lags are basically identical to those using the interval $[-50, +50]$ d.

For $\beta = 3$ d, local minima in D_4^2 play a role, while for $\beta > 10$ d, dispersion minima are not deep and delay uncertainties are relatively large. For $\beta = 4$ – 9 d, the time delay values are around 13–14 d with 1σ errors less than 2 d (see the bottom panel of Figure 2). We have then combined (averaged) these six precise delay measurements to obtain the 1σ confidence interval 13.5 ± 1.6 d (light-grey rectangle). The central values of the individual delays were averaged to find the mean value, and the uncertainty was computed as the square root of the sum of squares of two contributions: standard error of the mean value and average of individual delay errors.

The time delay of FBQ 0951+2635 was also measured from a variant of the χ^2 technique. The A image data were shifted by

a time lag τ and a microlensing polynomial of degree $N_{\text{ml}} = 5$, and then compared with B image data binned around the time-shifted dates of A. The bins with semisize α were constructed through a linear weighting function, and for a given value of α , we used a reduced chi-square (χ_r^2) minimisation to estimate the polynomial coefficients and time lag that make the shifted light curve of A and the binned brightness record of B to match (see details in Appendix A). We remark that a polynomial of degree $N_{\text{ml}} < 5$ leads to relatively high minimum χ_r^2 values, and the minimum χ_r^2 values for $N_{\text{ml}} = 5$ are barely modified by taking $N_{\text{ml}} = 6$. Thus, it is justified the choice $N_{\text{ml}} = 5$ when using the χ_r^2 method. The PyCS3 software⁴ (e.g., Tewes et al. 2013; Milon et al. 2020) includes another variant of the χ^2 technique to estimate time delays between images of gravitationally lensed quasars. However, the intrinsic variability is modelled as a free-knot spline, so we adopted a simpler scheme avoiding to fit a complex intrinsic signal.

For $3 < \alpha < 30$ d, the 1000 simulated light curves of each quasar image (see above) allowed us to calculate 1σ confidence intervals for the time delay (see Figure 3). We searched again for minima within the interval $[-30, +30]$ d, but checked the absence of border biases by using a second, more extended interval $[-50, +50]$ d for several α values. Excessively small or large values of α (or β for the minimum dispersion method; see above) are not suitable for time delay estimates. For $\alpha \geq 12$ d, χ_r^2 minima are affected by systematics (sudden drops in χ_r^2 at certain time lags) or are not deep. The mentioned systematics are responsible for the anomalous delay- α relationship for $\alpha = 12$ –16 d (see the black outlined rectangle in Figure 3). This anomaly consists of a set of formally ultra-precise delays around 14 d that are not consistent with each other. For $\alpha = 5$ –11 d, delay estimates are consistent with results from the dispersion technique, and the two most precise measurements (for $\alpha = 5$ and 11 d) are in excellent agreement with the dispersion-based delay of 13.5 ± 1.6 d. We also note that minima in χ_r^2 for $\alpha = 5$ and 11 d are derived from ~ 140 and ~ 190 AB data pairs, respectively, so there is a significant overlap between records of A and B.

2.3. Long-term microlensing

To trace the long-timescale extrinsic (microlensing) signal in red optical passbands, we built the difference light curve (DLC) from 1999 to 2024 (see Figure 4). This historical DLC relies on the *R*-band NOT-MT light curves and the GLENDAMA+ records in Figure 1, and it consists of differences between the image B magnitudes at original epochs and image A magnitudes shifted by the time delay $\Delta t = 13.5$ d, i.e., $m_B(t) - m_A(t - \Delta t)$. The differences were determined by linear interpolation of the time-shifted record of A. Figure 4 also displays dispersion-based solutions of the microlensing polynomial of degree five (thick solid line), which result from 1σ confidence intervals of polynomial coefficients for $3 < \beta < 30$ d. Although these solutions were obtained using only NOT and GLENDAMA+ data (filled circles), they predict reasonably well the DLC shape at intermediate epochs (open circles; however, as expected, the solutions do not account for the bump around day 53 000 reported by Shalyapin et al. 2009). The DLC has evolved from an initial value close to 1 mag at the end of the last century to 1.4–1.5 mag in the current decade. Hence, some recent DLC values are roughly consistent with the B/A flux ratio from radio observations and emission lines (see Sect. 3.1).

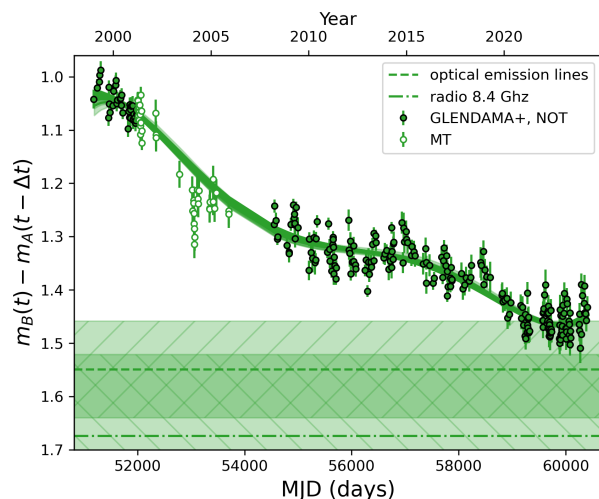


Fig. 4. New 25-yr DLC of FBQ 0951+2635 in red optical passbands from NOT-MT and GLENDAMA+ data. We also show solutions of the microlensing polynomial of degree five (thick solid line; see main text for details). For comparison purposes, we include magnitude differences from VLA data (horizontal dash-dotted line; Jakobsson et al. 2005) and emission lines (horizontal dashed line; see Sect. 3.1). The striped rectangles represent uncertainties in these two differences.

3. Observational constraints and structure of the main lensing galaxy

3.1. Observational constraints

We focus on the double quasar FBQ 0951+2635, giving here details on its observational constraints and summarizing them in Table 2. The spectroscopic redshifts of the source and the main lensing galaxy G are cited in Sect. 1. Jakobsson et al. (2005) and Sluse et al. (2012a) also used near-IR HST imaging (Kochanek et al. 2000) to determine the relative astrometry of the system and the morphology of the early-type galaxy G, whose brightness profile was modelled by a De Vaucouleurs law. However, the two independent analyses of the same data yielded two astrophotometric solutions (APS 1 and APS 2) that differ in image separation, i.e., angular distance between A and B, and galaxy morphological parameters (see Table 2). Additionally, the discovery paper (Schechter et al. 1998) reported VLA radio fluxes of both quasar images, which led to a radio flux ratio $B/A = 0.21 \pm 0.03$ ($m_B - m_A = 1.69 \pm 0.16$ mag) at 8.4 GHz (Jakobsson et al. 2005).

Using optical spectra of FBQ 0951+2635 from the Keck II Telescope (Schechter et al. 1998), the Very Large Telescope (Eigenbrod et al. 2007), and the William Herschel Telescope (Fian et al. 2021), we also estimated the flux ratio B/A for the cores of the C iv, C iii], and Mg II emission lines. The six B/A values range between 0.20 and 0.26, and a basic statistics of these six estimates (mean = 0.24 and standard deviation = 0.02, or equivalently, $m_B - m_A = 1.55 \pm 0.09$ mag) is in good agreement with the radio flux ratio (see above) and the macro-magnification ratio M in Table 4 of Sluse et al. (2012b). We then adopted Sluse et al.’s constraint on M . In addition to the spectroscopic test of the macro-magnification ratio, this paper presents a time delay measurement to $\sim 10\%$ by combining early optical light curves and those through observations made over the last 17 yr (see Sect. 2.2). In a near future, better photometric data in more densely sampled light curves might lead to a delay error less than 1.5 d. However, taking a possible microlensing-induced scatter

⁴ <https://gitlab.com/cosmograil/PyCS3>

Table 2. Summary of observational constraints of FBQ 0951+2635.

| Parameter (units) | Constraint | Reference |
|------------------------------------|----------------------|------------|
| z_s | 1.249 | 1 |
| z_l | 0.260 | 2 |
| APS 1 | | |
| x_A (") | 0.000 ± 0.001 | 3 |
| y_A (") | 0.000 ± 0.001 | 3 |
| x_B (") | -0.892 ± 0.001 | 3 |
| y_B (") | -0.628 ± 0.001 | 3 |
| x_G (") | -0.750 ± 0.002 | 3 |
| y_G (") | -0.459 ± 0.002 | 3 |
| e_G | 0.25 ± 0.04 | 3 |
| θ_{e_G} (°) | 22 ± 4 | 3 |
| R_G (") | 0.09 ± 0.02 | 3 |
| APS 2 | | |
| x_A (") | 0.0000 ± 0.0001 | 4 |
| y_A (") | 0.0000 ± 0.0001 | 4 |
| x_B (") | -0.8983 ± 0.0012 | 4 |
| y_B (") | -0.6336 ± 0.0012 | 4 |
| x_G (") | -0.7521 ± 0.0028 | 4 |
| y_G (") | -0.4603 ± 0.0028 | 4 |
| e_G | 0.47 ± 0.03 | 4 |
| θ_{e_G} (°) | 12.8 ± 2.2 | 4 |
| R_G (") | 0.78 ± 0.01 | 4 |
| M | 0.23 ± 0.02 | 5 |
| Δt (d) | 13.5 ± 1.6 | This paper |
| κ_{ext} | 0.23 | 6 |
| γ_{ext} | 0.04 | 6 |
| $\theta_{\gamma_{\text{ext}}}$ (°) | -44 | 6 |

Note: Here, z_s and z_l are the redshifts of the double quasar (images A and B) and the main lensing galaxy G, respectively. Additionally, regarding the two astro-photometric solutions APS 1 and APS 2, the brightest image A is located at the origin of coordinates, and the positive direction of x is defined by west, while the positive direction of y is defined by north. Some astrometric errors have also been made symmetric ($\sigma_x = \sigma_y$). The morphology of G (De Vaucouleurs brightness profile) is given by three parameters: ellipticity (e_G), position angle of the major axis (θ_{e_G} ; it is measured east of north), and effective radius (R_G). We also include the macro-magnification ratio M and time delay Δt with respect to the image A. All astro-photometric, magnification and delay constraints are 1σ confidence intervals. The last three rows correspond to the external convergence, external shear strength, and position angle of the external shear. We also assume a flat Λ CDM cosmology (see main text).

References. (1) Momcheva et al. (2015); (2) Eigenbrod et al. (2007); (3) Jakobsson et al. (2005); (4) Sluse et al. (2012a); (5) Sluse et al. (2012b); (6) Wilson et al. (2017).

of ~ 1 d into account (e.g., Tie & Kochanek 2018), this perspective may be excessively optimistic.

The time delay between the two images of a double quasar is basically given by the product of the time-delay distance and the Fermat potential variation between both images (e.g., Treu & Marshall 2016; Suyu et al. 2018). The Fermat potential variation relies upon the lensing mass distribution. In addition, the time-delay distance depends on z_s and z_l , and it is inversely proportional to H_0 , with other cosmological parameters playing a lesser role. For consistency with current constraints on secondary deflectors (see here below), we adopted a flat Λ CDM cosmology with $H_0 = 71 \text{ km s}^{-1} \text{ Mpc}^{-1}$, $\Omega_M = 0.274$, and $\Omega_\Lambda = 0.726$ (Hinshaw et al. 2009; Komatsu et al. 2009). Using these

cosmological parameters, Wilson et al. (2017) focused on determining the gravitational lensing effect of galaxy groups for FBQ 0951+2635, i.e., the group to which G belongs (environment of G) and additional line-of-sight groups. They did not explore the minor influence of isolated galaxies on the lensing potential, and estimated the typical values of the external convergence (κ_{ext}), external shear strength (γ_{ext}), and position angle of the external shear ($\theta_{\gamma_{\text{ext}}}$) that are shown in Table 2.

3.2. Methodology to reconstruct the mass distribution of the main deflector

The lensing mass distribution was initially modelled using two standard components: a singular power-law ellipsoid (SPLE) to describe the main lensing galaxy G and an external shear caused by the additional mass intervening (e.g., Suyu et al. 2013; Shajib et al. 2019). Although a SPLE is often characterised by its logarithmic mass-density slope γ , in this paper, we used the power-law index α_{pl} ($\alpha_{\text{pl}} = 3 - \gamma$) to avoid any confusion with the shear and to be consistent with the notation in the model catalog of the GRAVLENS/LENMODEL software (Keeton 2001, 2002). Despite neither the light nor the dark matter distribution in galaxies follow a power-law radial profile, the combined (total) density profile of G is expected to be close to isothermal (SPLE with $\alpha_{\text{pl}} \sim 1$; e.g., Koopmans et al. 2006; Capellari et al. 2015; Wang et al. 2020; Sheu et al. 2024). It is also noteworthy that the quasi-isothermal combined model leads to similar results than a model treating light and dark matter individually (e.g., Suyu et al. 2014; Millon et al. 2020b). For comparison purposes, we also considered a constant mass-to-light ratio model of G, i.e., a De Vaucouleurs (DV) surface mass density instead of that for a SPLE.

In addition to the power-law index, the parameters of the SPLE model are the 2D position (x_0, y_0), mass scale⁵ b , ellipticity e , and position angle θ_e . The external shear is also described by two parameters: strength γ_{ext} and position angle $\theta_{\gamma_{\text{ext}}}$, whereas it is not necessary to explicitly incorporate the external convergence into the lensing mass model. However, if $\kappa_{\text{ext}} \neq 0$, some model parameters must be appropriately reinterpreted (e.g., Falco et al. 1985; Grogin & Narayan 1996). We mean $b \mapsto b^* = b/(1 - \kappa_{\text{ext}})^{1/(2 - \alpha_{\text{pl}})}$ and $\gamma_{\text{ext}} \mapsto \gamma_{\text{ext}}^* = \gamma_{\text{ext}}/(1 - \kappa_{\text{ext}})$, as well as $H_0 \mapsto H_0^* = H_0/(1 - \kappa_{\text{ext}})$ (e.g., Fadelly et al. 2010). For example, for this system with such high external convergence (see Table 2), the use of H_0^* (instead of H_0) plays a critical role when the time delay is considered as a constraint on the mass distribution.

Setting the values of $z_s, z_l, \gamma_{\text{ext}}^*, \theta_{\gamma_{\text{ext}}}, H_0^*, \Omega_M$, and Ω_Λ , and taking 1σ confidence intervals for the positions of A, B and G, the macro-magnification, and the time delay (see Sect. 3.1), the GRAVLENS/LENMODEL software allowed us to fit the six parameters of the SPLE model (see above). Because we considered two astro-photometric solutions (APS 1 and APS 2), we obtained two different reconstructions of the SPLE mass distribution. We note again that it is the effective mass scale b^* which we fit in our model, so the true mass scale is derived from the product of b^* , and a scale factor depending on the parameters κ_{ext} and α_{pl} . In the least-squares fitting of the SPLE, the number of degrees of freedom (d.o.f.) was zero. Additionally, the constant mass-to-light ratio model (DV model) of G also contains six parameters: $x_0, y_0, b^*, e, \theta_e$, and the effective radius R . However, in this scenario, since light traces mass, we constrained the morphology of the DV mass ellipsoid from the 1σ confidence in-

⁵ The mass scale is defined in Eq. (26) of Keeton (2002). For a singular isothermal sphere, it equals the Einstein radius

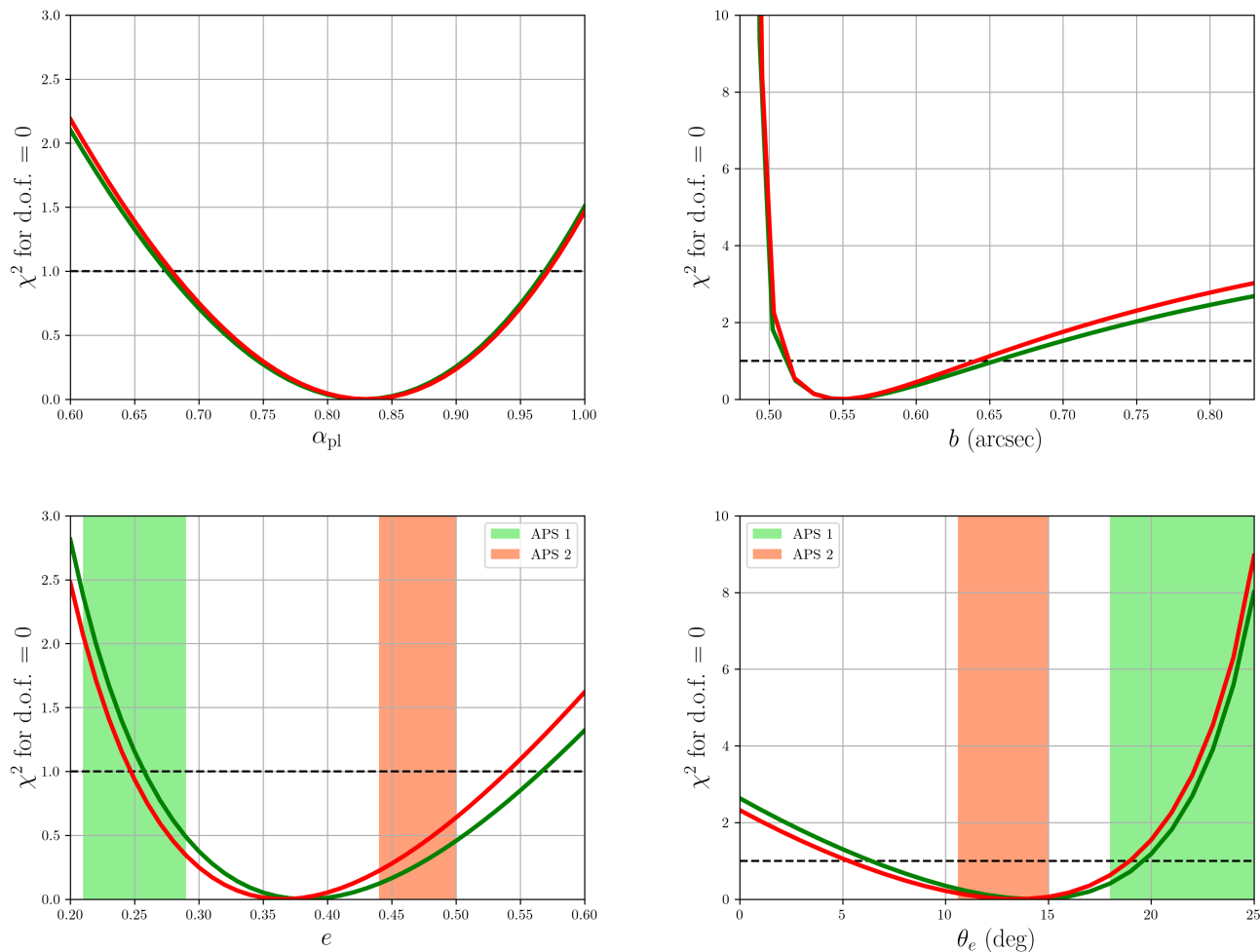


Fig. 5. SPLE parameters for the galaxy acting as main gravitational deflector to FBQ 0951+2635. Lines in green and red result from the astrometric constraints in APS 1 (see Table 2; Jakobsson et al. 2005) and APS 2 (see Table 2; Sluse et al. 2012a), respectively. *Top left panel:* power-law index. *Top right panel:* true mass scale. *Bottom left panel:* ellipticity of the mass distribution. *Bottom right panel:* position angle of the mass distribution. Our solutions for e and θ_e are also compared with the observed (near-IR) morphology of the galaxy. The light green and light salmon rectangles represent 1σ intervals in APS 1 and APS 2, respectively.

tervals of e_G , θ_{eG} , and R_G in Table 2. Thus, as a result of adding three more constraints, d.o.f. = 3.

3.3. Results

Using the SPLE mass model and astrometric constraints in APS 1, the 1σ intervals of the power-law index, true mass scale, ellipticity and position angle are $\alpha_{pl} = 0.822 \pm 0.147$, $b (") = 0.585 \pm 0.073$, $e = 0.412 \pm 0.155$, and $\theta_e (^\circ) = 13.0 \pm 6.6$. These results are very similar to those using astrometric constraints in APS 2: $\alpha_{pl} = 0.825 \pm 0.146$, $b (") = 0.577 \pm 0.064$, $e = 0.394 \pm 0.147$, and $\theta_e (^\circ) = 12.2 \pm 6.9$. In both cases, we obtain best fits with $\chi^2 \sim 10^{-5}$ (d.o.f. = 0). Figure 5 also depicts $\chi^2 - \alpha_{pl}$, $\chi^2 - b$, $\chi^2 - e$, and $\chi^2 - \theta_e$ relationships from the two astrometric datasets. As expected, there is only a small deviation from isothermality ($\alpha_{pl} = 1$; see Sect. 3.2). Additionally, light and mass are closely aligned, since the mass ellipticity and its orientation agree reasonably well with their near-IR counterparts.

We have shown that the SPLE-based reconstruction of the galaxy mass is very weakly influenced by the difference between image separation in APS 1 and APS 2. Moreover, despite discrepancies between the galaxy shape in these two datasets ($\sim 6\sigma$

in e_G and $\sim 3\sigma$ in θ_{eG}), if formal errors are taking into account, both (e_G, θ_{eG}) measurements are consistent with the (e, θ_e) solutions from the SPLE mass model (see Figure 5). Our lensing mass modelling focuses on the use of a Hubble constant that corresponds to an average of the main measurements from different experiments ($H_0 = 71 \text{ km s}^{-1} \text{ Mpc}^{-1}$; e.g., Di Valentino et al. 2021) and typical values of the constraints on secondary deflectors for this concordance H_0 . Therefore, accounting for current uncertainties in H_0 and the effects by secondary deflectors increases the error bars of α_{pl} , b , e , and θ_e , but does not modify their best-fit values. As an example, a reasonable H_0 interval of 68 to 74 $\text{km s}^{-1} \text{ Mpc}^{-1}$ (e.g., Di Valentino et al. 2021) increases uncertainties in α_{pl} by about 6.5%. These enlargements are similar to those associated with the errors in κ_{ext} and γ_{ext} (the error in $\theta_{\gamma_{\text{ext}}}$ is not mentioned; Wilson et al. 2017), and clearly below the 18% uncertainties estimated for α_{pl} .

We also considered the DV mass model and all (astrometric and morphological) constraints in APS 1 and APS 2. Interestingly, the DV mass distribution is reasonably consistent with the constraints in APS 2 ($\chi^2 \sim 3.7$), suggesting that a constant mass-to-light ratio galaxy cannot be ruled out (see also Magain & Chantry 2013). The best-fit solution includes a true mass scale

of $1''.12$ and reproduces well the morphological measurements of Sluse et al. ($e = 0.45$, $\theta_e = 13.0^\circ$, and $R = 0''.78$). However, using APS 1, we do not achieve a good solution for the lensing mass because $\chi^2 \sim 175$ is much higher than d.o.f. = 3 (see the end of Sect. 3.2). This high χ^2 value is largely due to the morphological constraints in APS 1, and the main difference between the two light distributions of G lies in the effective radius: R_G in APS 2 is one order of magnitude larger than R_G in APS 1.

To decide whether or not light is an acceptable tracer of the mass in the galaxy at redshift 0.26, we have reanalysed the HST archival data of FBQ 0951+2635, paying special attention to the value of the effective radius. The central idea was to repeat Jakobsson et al.'s evaluation of R_G , who used a technique less refined than that of the COSMOGRAIL project (Sluse et al. 2012a). More specifically, we taken the NICMOS drizzled frame in the *H* band and used the *A* image as an empirical point spread function (as Jakobsson et al.'s did), and then applied the IMFIT-FITS software (McLeod et al. 1998) by setting the positions of *A* and *B* at the values cited by Jakobsson et al. (2005). For a DV brightness profile, our approach yields an effective radius significantly larger than that estimated by Jakobsson et al. and closer to Sluse et al.'s measurement. Jakobsson et al. most likely underestimated the effective radius, while Sluse et al.'s solution for R_G relies on an iterative MCS deconvolution algorithm (Chantry & Magain 2007) and seems much more reliable. Hence, we cannot rule out a constant mass-to-light ratio DV model.

4. Conclusions

Prior to this work, optical, near-IR and radio observations towards the doubly imaged quasar FBQ 0951+2635 have provided a rich set of constraints for the gravitational lens system. However, unfortunately, early optical monitoring in the period 1999–2001 did not lead to a reliable time delay between the two quasar images (e.g., Jakobsson et al. 2005; Eulaers & Magain 2011; Rathna Kumar et al. 2015), which is a key constraint to "blindly" reconstruct the mass structure of the main lensing galaxy G, i.e., its mass scale and morphology, or to be used for time-delay cosmography (e.g., Birrer et al. 2024). Here, we focus on a robust determination of the time delay and a discussion of the structure of the non-local early-type galaxy G (e.g., Kochanek et al. 2000; Eigenbrod et al. 2007).

We consider new optical light curves in the period 2008–2024, including significant intrinsic fluctuations and consisting of quasar image magnitudes at 213 epochs. These GLENDAMA+ records are merged together with the early ones, and we then use two different cross-correlation techniques to match the light curves of both images by allowing for a time delay and microlensing polynomial variability. We also present easy-to-use Python scripts associated with the two techniques and obtain a time delay of 13.5 ± 1.6 d (1σ confidence interval). This reliable measurement to $\sim 10\%$ resolves the long-standing controversy over the time delay of FBQ 0951+2635. In addition, a microlensing polynomial of degree five describes well the long-timescale evolution of the difference light curve. We also note that the current optical-passband flux ratio is close to the macro-magnification ratio.

Most previous reconstructions of the mass of G from a SPLE model were based on the assumption of isothermality ($\alpha_{\text{pl}} = 1$), and priors on e and θ_e from the observed light structure (e.g., Sluse et al. 2012a). However, it is possible to "blindly" fit parameters of the mass structure of G by knowing 1σ intervals for the positions of quasar images and G, the macro-magnification ratio, and the time delay, along with typical values of the source

and lens redshifts, the convergence and shear due to secondary gravitational deflectors, and the main cosmological parameters. We mean that for a SPLE mass model, hypotheses/priors on α_{pl} , e and θ_e are not required. Additionally, the effective mass scale arising from the SPLE model fitting can be converted into a true mass scale of G. Thus, the constraints in Table 2 lead to SPLE mass solutions with a deviation from isothermality consistent with studies of lensing galaxies selected from the SLACS Survey (Koopmans et al. 2006; Barnabè et al. 2009; Koopmans et al. 2009). As expected, we also find good alignment between the mass distribution and the near-IR light of G (e.g., Koopmans et al. 2006). We also note that a DV mass model (constant mass-to-light ratio galaxy) cannot be ruled out from current data.

The observational constraints in Table 2 can be used to take a deeper look at the mass structure of G by considering models of the galaxy other than the SPLE and DV (e.g. Schneider & Sluse 2013; Kochanek 2020). For example, light-based priors on e and θ_e allow one to study mass models incorporating two more parameters. New observations of the lens system will also contribute to a better understanding of the galaxy structure, opening the door to the analysis of its mass distribution from accurate non-parametric reconstructions (e.g., Saha & Williams 1997; Diego et al. 2005). Future observations should include spatially resolved stellar kinematics of G, and detailed imaging of the lensing galaxy and the lensed host galaxy of the quasar. In particular, new near-IR imaging along with state-of-the-art analysis techniques should definitively resolve the controversy over the light structure of the galaxy (Jakobsson et al. 2005; Sluse et al. 2012a; Rivera et al. 2023).

Acknowledgements. The Liverpool Telescope (LT) is operated on the island of La Palma by Liverpool John Moores University in the Spanish Observatorio del Roque de los Muchachos of the Instituto de Astrofísica de Canarias with financial support from the UK Science and Technology Facilities Council. We thank the staff of the LT for a kind interaction. We also thank the anonymous referee for providing valuable feedback on the original manuscript. VNS acknowledges the Universidad de Cantabria (UC) and the Spanish Agencia Estatal de Investigación (AEI) for financial support for a long stay at the UC in the period 2022–2024. This research has been supported by the grant PID2020-118990GB-I00 funded by MCIN/AEI/10.13039/501100011033.

References

- Abbott, T. M. C., Adamów, M., Aguena, M., et al. 2021, *ApJS*, 255, 20
 Barnabè, M., Czoske, O., Koopmans, L. V. E., et al. 2009, *MNRAS*, 399, 21
 Birrer, S., Shajib, A. J., Galan, A., et al. 2020, *A&A*, 643, A165
 Birrer, S., Millon, M., Sluse, D., et al. 2024, *Space Sci. Rev.*, 220, 48
 Capellari, M., Romanowsky, A. J., Brodie, J. P., et al. 2015, *ApJ*, 804, L21
 Chantry, V., & Magain, P. 2007, *A&A*, 470, 467
 Di Valentino, E., Mena, O., Pan, S., et al. 2021, *Class. Quant. Grav.*, 38, 153001
 Diego, J. M., Protopapas, P., Sandvik, H. B., & Tegmark, M. 2005, *MNRAS*, 360, 477
 Eigenbrod, A., Courbin, F., & Meylan, G. 2007, *A&A*, 465, 51
 Eulaers, E., & Magain, P. 2011, *A&A*, 536, A44
 Fadely, R., Keeton, C. R., Nakajima, R., & Bernstein, G. M. 2010, *ApJ*, 711, 246
 Falco, E. E., Gorenstein, M. V., & Shapiro, I. I. 1985, *ApJ*, 289, L1
 Fian, C., Mediavilla, E., Motta, V., et al. 2021, *A&A*, 653, A109
 Flewelling, H. A., Magnier, E. A., Chambers, K. C., et al. 2020, *ApJS*, 251, 7
 Gil-Merino, R., Goicoechea, L. J., Shalyapin, V. N., & Oscoz, A. 2018, *A&A*, 616, A118
 Goicoechea, L. J., & Shalyapin, V. N. 2016, *A&A*, 596, A77
 Grogin, N. A., & Narayan, R. 1996, *ApJ*, 464, 92
 Hinshaw, G., Weiland, J. L., Hill, R. S., et al. 2009, *ApJS*, 180, 225
 Jakobsson, P., Hjorth, J., Burud, I., et al. 2005, *A&A*, 431, 103
 Keeton, C. R. 2001, arXiv:astro-ph/0102340v1
 Keeton, C. R. 2002, arXiv:astro-ph/0102341v2
 Kochanek, C. S. 2020, *MNRAS*, 493, 1725
 Kochanek, C. S., Falco, E. E., Impey, C. D., et al. 2000, *ApJ*, 543, 131 (CASTLeS database at <https://lweb.cfa.harvard.edu/castles/>)
 Komatsu, E., Dunkley, J., Nolte, M. R., et al. 2009, *ApJS*, 180, 330

- Koopmans, L. V. E., Treu, T., Bolton, A. S., Burles, S., & Moustakas, L. A. 2006, *ApJ*, 649, 599
- Koopmans, L. V. E., Bolton, A., Treu, T., et al. 2009, *ApJ*, 703, L51
- Magain, P., & Chantry, V. 2013, arXiv:astro-ph/1303.6896v1
- McLeod, B. A., Bernstein, G. M., Rieke, M. J., & Weedman, D. W. 1998, *AJ*, 115, 1377
- Metcalf, R. B., & Madau, P. 2001, *ApJ*, 563, 9
- Millon, M., Courbin, F., Bonvin, V., et al. 2020, *A&A*, 640, A105
- Millon, M., Galan, A., Courbin, F., et al. 2020b, *A&A*, 639, A101
- Momcheva, I. G., Williams, K. A., Cool, R. J., Keeton, C. R., & Zabludoff, A. I. 2015, *ApJS*, 219, 29
- Moustakas, L. A., & Metcalf, R. B. 2003, *MNRAS*, 339, 607
- Paraficz, D., Hjorth, J., Burud, I., Jakobsson, P., & Elíasdóttir, Á. 2006, *A&A*, 455, L1
- Pelt, J., Kayser, R., Refsdal, S., & Schramm, T. 1996, *A&A*, 305, 97
- Planck Collaboration VI. 2020, *A&A*, 641, A6
- Rathna Kumar, S., Stalin, C. S., & Prabhu, T. P. 2015, *A&A*, 580, A38
- Refsdal, S. 1964, *MNRAS*, 128, 307
- Rivera, A. B., Morgan, C. W., Florence, S. M., et al. 2023, *ApJ*, 952, 54
- Rusu, C. E., Fassnacht, C. D., Sluse, D., et al. 2017, *MNRAS*, 467, 4220
- Saha, P., & Williams, L. L. R. 1997, *MNRAS*, 292, 148
- Schechter, P. L., Gregg, M. D., Becker, R. H., Helfand, D. J., & White, R. L. 1998, *AJ*, 115, 1371
- Schneider, P., & Sluse, D. 2013, *A&A*, 559, A37
- Shajib, A. J., Birrer, S., Treu, T., et al. 2019, *MNRAS*, 483, 5649
- Shajib, A. J., Mozumdar, P., Cheng, G. C.-F., et al. 2023, *A&A*, 673, A9
- Shajib, A. J., Vernardos, G., Collett, T. E., et al. 2024, *Space Sci. Rev.*, 220, 87
- Shalyapin, V. N., & Goicoechea, L. J. 2017, *ApJ*, 836, 14
- Shalyapin, V. N., Goicoechea, L. J., Koptelova, E., et al. 2009, *MNRAS*, 397, 1982
- Sheu, W., Shajib, A. J., Treu, T., et al. 2024, arXiv:astro-ph/2408.10316
- Sluse, D., Chantry, V., Magain, P., Courbin, F., & Meylan, G. 2012a, *A&A*, 538, A99
- Sluse, D., Hutsemékers, D., Courbin, F., Meylan, G., & Wambsganss, J. 2012b, *A&A*, 544, A62
- Suyu, S. H., Marshall, P. J., Auger, M. W., et al. 2010, *ApJ*, 711, 201
- Suyu, S. H., Auger, M. W., Hilbert, S., et al. 2013, *ApJ*, 766, 70
- Suyu, S. H., Treu, T., Hilbert, S., et al. 2014, *ApJ*, 788, L35
- Suyu, S. H., Chang, T.-C., Courbin, F., & Okumura, T. 2018, *Space Sci. Rev.*, 214, 91
- Tewes, M., Courbin, F., & Meylan, G. 2013, *A&A*, 553, A120
- Tie, S. S., & Kochanek, C. S. 2018, *MNRAS*, 473, 80
- Treu, T., & Marshall, P. J. 2016, *A&ARv*, 24, 11
- Wang, Y., Vogelsberger, M., Xu, D., et al. 2020, *MNRAS*, 491, 5188
- Wilson, M. L., Zabludoff, A. I., Keeton, C. R., et al. 2017, *ApJ*, 850, 94
- Wong, K. C., Suyu, S. H., Cheng, G. C.-F., et al. 2020, *MNRAS*, 498, 1420

Appendix A: Easy-to-use software for time delay estimation in presence of microlensing

We consider a double quasar with images A and B. The A image magnitudes at observing times t_i ($i = 1, \dots, N_A$) are given by $A_i = m_A(t_i)$, whereas $B_j = m_B(t_j)$ at observing times t_j ($j = 1, \dots, N_B$) represent the light curve of B. The A image data are shifted by a time lag τ and a microlensing polynomial of degree N_{ml} , and then compared to the B image data. The microlensing polynomial

$$P(t_i) = a_0 + a_1 t_i + a_2 t_i^2 + \dots + a_{N_{\text{ml}}} t_i^{N_{\text{ml}}} \quad (\text{A.1})$$

is characterised by coefficients a_k ($k = 0, \dots, N_{\text{ml}}$), and the central idea is to find the values of (τ, a_k) that provide the best match between the shifted light curve of A and the original light curve of B.

To estimate best values of (τ, a_k) , we minimise two different merit functions: dispersion D_4^2 and reduced chi-square χ_r^2 (see main text and here below). Two main advantages of using a polynomial function to account for the microlensing variability are the possibility to describe a very general behaviour and the linear role of polynomial coefficients in merit functions. Thus, for each value of τ , we can optimise the linear parameters a_k analytically, so multivariable merit functions are reduced to 1D spectra depending on the non-linear parameter τ . Minima of these 1D spectra yield estimates of the time delay between A and B. We also note that Python scripts to use both techniques (merit functions) are available at the GitHub repository URL https://github.com/glendama/q0951time_delay, and draw attention to the fact that the so-called polynomial order in the scripts (Nord) equals $N_{\text{ml}} + 1$.

Appendix A.1: Minimum dispersion method

The merit function is given by

$$D_4^2(\tau, a_k) = \frac{\sum_i \sum_j W_{ij} S_{ij} [A_i - B_j + P(t_i)]^2}{\sum_i \sum_j W_{ij} S_{ij}}, \quad (\text{A.2})$$

where $W_{ij} = 1/(\sigma_{A_i}^2 + \sigma_{B_j}^2)$ are statistical weights computed from photometric errors and $S_{ij} = \exp[-(t_i - t_j + \tau)^2/\beta^2]$ are weights for time separations. Our time-separation weighting scheme relies on a Gaussian function and a "decorrelation length" β , and it is inspired by Eq. (13) of Pelt et al. (1996).

For each value of τ , the minimisation of the dispersion with respect to the polynomial coefficients, i.e., $\partial D_4^2/\partial a_k = 0$, produces the system of linear equations

$$\sum_i \sum_j W_{ij} S_{ij} \sum_l t_i^{l+k} a_l = - \sum_i \sum_j W_{ij} S_{ij} (A_i - B_j) t_i^k. \quad (\text{A.3})$$

This system of $N_{\text{ml}} + 1$ equations can be solved by standard procedures of linear algebra, yielding a set of optimal microlensing coefficients a_k for each time lag and the corresponding dispersion spectrum $D_4^2(\tau)$.

Appendix A.2: Reduced chi-square minimisation

The merit function has the form

$$\chi_r^2(\tau, a_k) = \frac{1}{N_{\text{pair}} - (N_{\text{ml}} + 2)} \sum_i W_i [A_i - B'_i + P(t_i)]^2, \quad (\text{A.4})$$

where B'_i is the B image magnitude binned around $t_i + \tau$ to build the (A_i, B'_i) pair, N_{pair} is the total number of AB' pairs for the time

lag τ ($i = 1, \dots, N_{\text{pair}}$), and $W_i = 1/(\sigma_{A_i}^2 + \sigma_{B'_i}^2)$ is the inverse of the sum of squared uncertainties. To build the bin in B around $t_i + \tau$, we use a linear weighting function $1 - |t_i - t_j + \tau|/\alpha$ for dates t_j verifying $|t_i - t_j + \tau| \leq \alpha$.

The minimisation with respect to the microlensing coefficients a_k yields the linear system

$$\sum_i W_i \sum_l t_i^{l+k} a_l = - \sum_i W_i (A_i - B'_i) t_i^k, \quad (\text{A.5})$$

and thus optimal values of a_k for each time lag and the 1D spectrum $\chi_r^2(\tau)$.